Combined Navier-Stokes and Species Transport with Application to Flow Batteries

Tyler Olsen

May 11, 2014

1 Flow Battery Introduction

As renewable energy sources such as wind and solar power are becoming more viable, there has been a significant push to integrate them into the power grid. However, many of these renewable sources are transient, meaning that they cannot be relied upon to provide a constant, controlled power output at all times. Because of this, traditional power plants must be able to account for the fluctuations in power demand, however, doing so puts extraordinary strain on the power plants. Therefore, having a way to buffer the transient power sources during times of excess supply (sun/wind) and to dispense the stored energy during times of deficient supply could mitigate the damage to traditional power plants.

One obvious approach is to use a battery as this buffer, but traditional batteries cannot be scaled to the required capacity. Some companies, such as A123 Energy Solutions, have tried to circumvent this limitation by essentially filling a cargo container with smaller batteries. While this approach has been shown to be successful, a better solution is believed to exist.

One such solution is the "flow battery." This configuration differs from a traditional battery by separating the storage areas and reaction areas of the battery. This is illustrated in the schematics in figure 1. The flow battery configuration allows you to pump non-reacted anolyte/catholyte solutions into the reaction area of the battery from a tank, where the normal chemical reactions take place, and the spent material is pumped into collection tanks. This allows the battery to be scaled as large as the application requires.

Since detailed experimental data is not yet available for the materials being used in the actual flow battery project occuring at MIT, parameters for the various equations were chosen so that the solutions exhibited "interesting" behavior. That is, for the concentration field, parameters were chosen so that both diffusion and convection were important, and neither transport mechanism dominated the problem. The non-dimensional group corresponding to this condition is called the Peclet number. The Peclet number is defined as

$$Pe = \frac{LU}{D} \tag{1}$$

where L, U, and D are characteristic length, velocity, and diffusion coefficient scales respectively. A large Peclet number ($Pe \gg 1$) indicates that convection dominates. A small Peclet number ($Pe \ll 1$) indicates that diffusion dominates the solution.

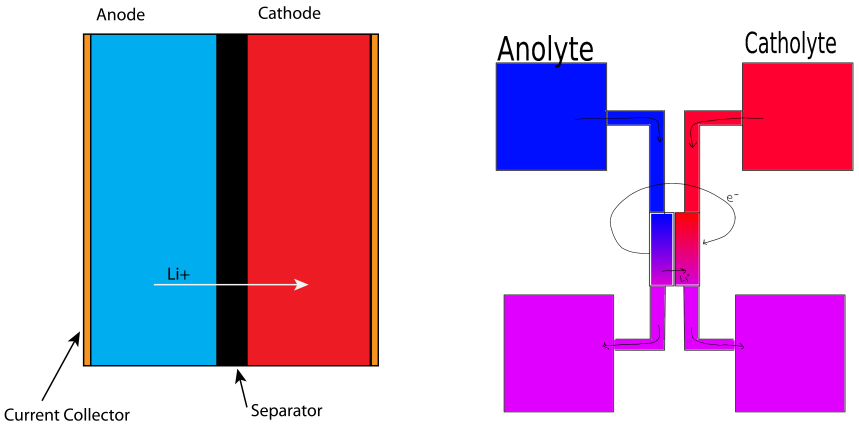

Figure 1: Left: schematic of a traditional galvanic cell. Right: schematic of flow battery.

2 Flow Battery Mathematical Model

The numerical model of the flow battery consists of solving a fluid flow problem coupled to an advection-diffusion-reaction equation for species concentration. The species concentration represents the concentration of reactants in the solution which can participate in the reduction-oxidation (redox) reactions that take place inside the battery. Therefore, the following equations must be solved simultaneously:

$$\rho \frac{\partial \mathbf{u}}{\partial t} + \rho \left(\nabla \mathbf{u} \right) \mathbf{u} = -\nabla P + \mu \nabla^2 \mathbf{u} \tag{2}$$

$$\nabla \cdot \mathbf{u} = 0 \tag{3}$$

$$\frac{\partial c}{\partial t} + \mathbf{u} \cdot (\nabla c) = Q + D \nabla^2 c \tag{4}$$

Equation (2) is the Navier-Stokes equation for an incompressible Newtonian fluid. This can be derived from a more general statement of linear momentum balance. In this equation, ρ is the mass density per unit volume, μ is the dynamic viscosity, P is the pressure field, and $\mathbf{u}$ is the velocity field. Equation (3) is the incompressibility constraint on the fluid velocity field.

Equation (4) is the transport equation for the scalar species concentration in an incompressible flow field. In this equation, c is the species concentration, D is the diffusivity, and Q

is the volumetric chemical reaction rate. This can be derived from the scalar continuity equation using Fick's law of diffusion

$$\frac{\partial c}{\partial t} + \nabla \cdot \mathbf{j} = Q \tag{5}$$

where $\mathbf{j} = (-D\nabla c + \mathbf{u}c)$ is the flux of c into a differential volume. The volumetric reaction rate Q represents the rate at which reactants turn into products. In a real battery system, Q can be a complicated function related to the voltage of the battery, electronic conductivity of the solution, ionic conductivity of the solution, and other factors. For the sake of constructing a simple model, however, the reaction rate Q will be taken to be proportional to the local concentration of reactant

$$Q = -k \cdot c \tag{6}$$

where k is a positive rate constant. This is not an unrealistic assumption to make, as it implies that at any given time, each molecule of reactant has the same probability of turning into product. It is a form often used in non-battery systems to model the concentration of a chemical species over time.

The following sections will address the numerical solution of these partial differential equations.

3 Navier-Stokes Solver

The first task in modeling the flow battery is to solve the fluid flow equations. There are multiple ways to solve the incompressible Navier-Stokes equations, so one was selected that works equally well in 2D and 3D, thus ruling out the vorticity/stream-function formulation. The method chosen was the projection method originally formulated by Chorin in 1967 [1].

3.1 Chorin's Projection Method

The projection method is a procedure to solve the incompressible Navier-Stokes equations using the primitive $\mathbf{u}$ and P variables, rather than solving solving for the vorticity and stream function ($\omega - \Psi$ formulation) and post-processing for the velocity field. This has the advantage of being equally simple to implement in 3D as in 2D, a feature that the $\omega - \Psi$ formulation does not have. Another feature of the method is that the incompressibility constraint is enforced exactly at every time step. The method relies on the Helmholtz decomposition of a vector field into divergence-free and curl-free parts. The algorithm can be illustrated using a semi-discretized form of the NS equations

$$\frac{\mathbf{u}^{n+1} - \mathbf{u}^*}{\Delta t} - \frac{\mu}{\rho}\nabla^2 \mathbf{u}^* = -(\nabla \mathbf{u}^n)\mathbf{u}^n \tag{7}$$

where $\mathbf{u}^*$ is an intermediate velocity field that does not satisfy the incompressibility constraint and supersctipt n and $n+1$ refer to the nth and $(n+1)$th timestep. Written this way, the following relation holds:

$$\mathbf{u}^* = \mathbf{u}^{n+1} + \frac{\rho}{\Delta t}\nabla P^{n+1} \tag{8}$$

Now the incompressibility constraint is enforced by taking the divergence of (8).

$$\nabla^2 P^{n+1} = \frac{\Delta t}{\rho}\nabla \cdot \mathbf{u}^* \tag{9}$$

Equation (9) can be solved to find the pressure field that enforces an incompressible velocity field at time t_{n+1}. This pressure field can then be substituted into (8) to find the new velocity field.

3.2 Staility

The stable time step may be obtained by analysis of simpler problems. First and foremost, the Navier-Stokes are a combination of a one-way wave equation and a diffusion equation. Therefore, a time step satisfying the stability of both of these problems individually will be stable overall.

3.2.1 Wave Equation Stability

Velocity gradients were computed using an upwind one-sided difference. The relavent wave equation to analyze for stability here is

$$\frac{u^{n+1} - u^n}{\Delta t} - c\frac{u^n_{i+1} - u^n_i}{\Delta x} = 0 \tag{10}$$

where c is the wave speed. By performing Von-Neumann stability analysis on this finite difference equation, one can see that the stable timestep is

$$\Delta t < \frac{\Delta x}{c} \tag{11}$$

In the Navier-Stokes equation, the wave speed is equal to the maximum velocity in the problem. Using this to calculate the time step ensures that the problem is stable on the whole domain.

3.2.2 Diffusion Equation Stability

The diffusion equation appears in the Navier-Stokes equations through the $\nabla^2\mathbf{u}$ term. The stable time step can again be computed using Von-Neumann stability analysis. The stablility will be shown for both explicit and implicit schemes to justify the choice of integrating (7) implicitly.

For explicit integration:

$$\begin{aligned}\frac{\partial u}{\partial t} &= D\nabla^2 u \\ \frac{u^{n+1}-u^n}{\Delta t} &= \frac{D}{\Delta x^2}\left(u_{i+1}^n + u_{i-1}^n - 2u_i^n\right)\end{aligned}$$

Following the growth of a Fourier mode $u = e^{ikx}$ and defining the growth factor $G = u^{n+1}/u^n$:

$$(G-1) = \frac{\Delta t D}{\Delta x^2}\left(2\cos(\theta) - 2\right)$$

The requirement for stability is that $|G| < 1$. The stable Δt is therefore bounded by the inequality

$$\Delta t < \frac{\Delta x^2}{2D} \tag{12}$$

The scaling of the time step with Δx^2 is unacceptable for simulations on fine grids where Δx is very small. This would lead to computation times that are excessively long. To remedy this problem, consider implicit integration:

$$\begin{aligned}\frac{\partial u}{\partial t} &= D\nabla^2 u \\ \frac{u^{n+1}-u^n}{\Delta t} &= \frac{D}{\Delta x^2}\left(u_{i+1}^{n+1} + u_{i-1}^{n+1} - 2u_i^{n+1}\right)\end{aligned}$$

Doing the same operation as above with the Fourier modes, we obtain

$$G - 1 = G\frac{\Delta t D}{\Delta x^2}\left(2\cos(\theta) - 2\right)$$

Now, when the constraint $|G| < 1$ is applied, we find that it is satisfied for any choice of Δt.

3.3 Performance on benchmark problems

In order to ensure the correctness of the Navier-Stokes solver, simulations were run on benchmark problems and compared with theoretical or published solutions. First, simple pressure-driven flow between parallel plates was analyzed because it has a known analytical solution. Next, the solution to 2D lid-driven cavity flow was compared to simulations run by Ghia *et al* [2].

3.3.1 Parallel Plate Flow

The simples benchmark problem was that of pressure-driven flow between parallel plates. The top and bottom plates have no-slip boundary conditions, and the inlet and outlet have pressure boundary conditions. Figire 2 shows a schematic of the problem.

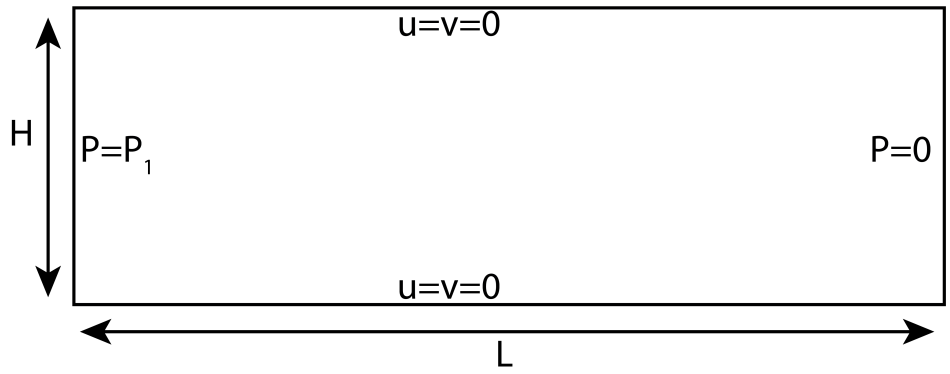

Figure 2: Schematic of the pressure-driven parallel plate flow problem

The steady horizontal velocity field for this problem can be analytically obtained by removing the transient terms from the Navier-Stokes equations and assuming that the x-velocity field only has nonzero derivatives in the y-direction. The solution to this differential equation with the appropriate boundary conditions is

$$u_x(y) = \frac{1}{2\mu}\frac{P_1}{L}\left(Hy - y^2\right) \tag{13}$$

Figure 3 shows a comparison of the velocity profile at the $x = L/2$ cross-section between the simulation results and the analytical solution.

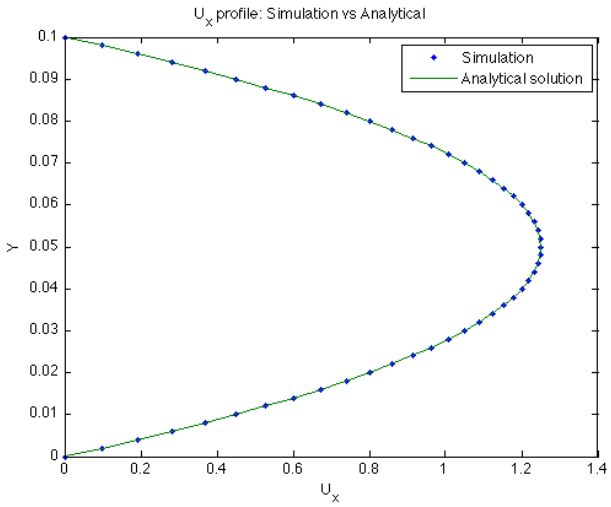

Figure 3: Comparison between simulation and analytical velocity profile.

The maximum velocity occurs at the centerline, and has the value $u_x(H/2) = P_1 H^2/(8\mu L)$. Simuations were run using the values $\mu = 1$, $L = 1$, $P_1 = 1000$, $H = 0.1$ and the velocity error was computed at the centerline. The results of the simulations are below in table 1. The table shows that the simulations converge to zero error. The order of convergence is approximately 1.

N_y	error
25	0.0021
51	0.0012
75	0.0009

Table 1: Centerline velocity error vs mesh density in y-direction

3.3.2 Lid-driven cavity flow

The second benchmark problem is that of 2D lid-driven cavity flow. This has no analytical solution, but the problem has been thoroughly studied both experimentally and numerically and has been well-documented in the literature. The results from this study were compared against those of Ghia *et al* [2].

The lid-driven cavity problem is a problem where the entire boundary is given dirichlet boundary conditions—that is, all components of velocity are prescribed over the entire boundary. The domain is an $L \times L$ square, and no-slip boundary conditions are applied to the sides and bottom. The x-velocity is nonzero on the top, while the y-velocity is held to zero. These are illustrated graphically in figure 4. It is important to note that, although the terms "lid-driven cavity" and "shear-driven cavity" are often used interchangeably, the shear-driven cavity problem imposes a traction on the top rather than a velocity.

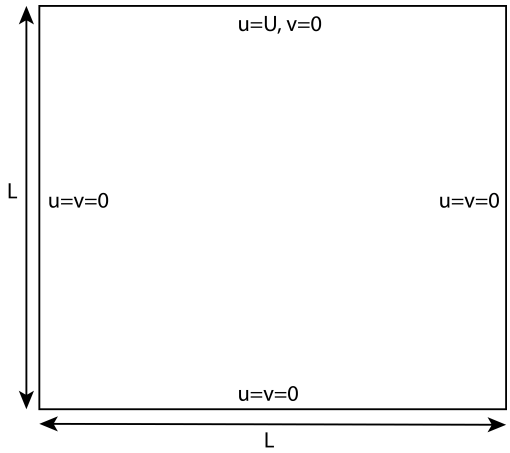

Figure 4: Schematic of the lid-driven cavity domain with boundary conditions

In order to assess the performance of the solver, simulations were run at multiple Reynolds numbers and at multiple grid densities. Ghia *et al* published the x-velocity data at selected points on a vertical line through the geometric center of the domain at several values of Re, where $Re = UL/\nu$. The solver was run until a steady-state solution was obtained at $Re = 100$, 400, and 1000, and the results were compared against their data. A plot of the comparison can be found below in figure 5. It can be seen that the published results are virtually indistinguishable from the current study at every value of Re.

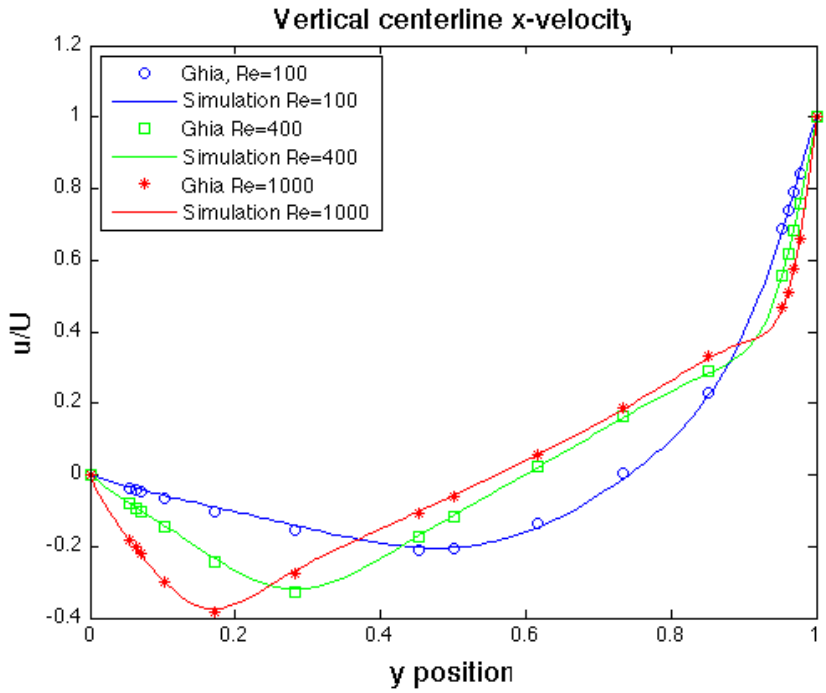

Figure 5: Comparison of results against published data from [2]

4 Species Transport

4.1 Finite Difference Discretization

The scalar transport equation was discretized using similar operators as the Navier-Stokes equations. Gradients were approximated by 1st order upwind derivatives, and the laplacian was approximated by the 2nd order centered laplacian. The time derivative was approximated by the 1st order difference.

$$\frac{\partial c(\mathbf{x})}{\partial t} = \frac{c_{i,j}^{n+1} - c_{i,j}^{n}}{\Delta t} \tag{14}$$

The equation was integrated using 1st order implicit time integration. Higher order accuracy was not considered for this PDE since the Navier-Stokes solver is only first-order accurate. By using implicit time stepping rather than explicit time stepping, the stable time step was proportional to Δx rather than Δx^2. See the above analysis of stable time steps for explicit and implicit schemes for a derivation of this.

4.2 Geometry and Boundary Conditions

The system was solved using the parallel plate geometry described above. The boundary conditions for the fluid flow are the same as above. The boundary conditions for the concentration field are:

- $c = c_1$ at $x = 0$
- No flux at $y = 0$ and $y = H$
- Outflow conditions at $x = L$: species were allowed to be carried out by the fluid flow

The concentration field was initialized to zero everywhere, but this does not impact the steady state solution.

4.3 Steady State Solution

As mentioned in the introduction, exact material parameters are not known for the components of the flow battery system. For this reason, parameters were chosen so that $Pe \sim 1$. This ensures that both diffusion and convection play a significant role in the solution. To satisfy this, the diffusion coefficient D in (4) was chosen to be $D = 0.01$. Pressures at the inlet were chosen over the interval $P_1 \in [100, 2000]$. Upon post-processing, the Peclet numbers ranged from 1.25 to 25.0. The values of the other parameters are $\mu = 1$, $\rho = 1000$, $k = 1$.

The flow field for the coupled problem is the same as in parallel plate flow. See figure 3 for a plot of the velocity profile at any value of x.

The concentration field varied in both the x and y directions. A contour plot of a concentration field can be found below in figure 6. Since the concentration field is highly dependant on the velocity field via the inlet pressure, the contour is simply a representative field.

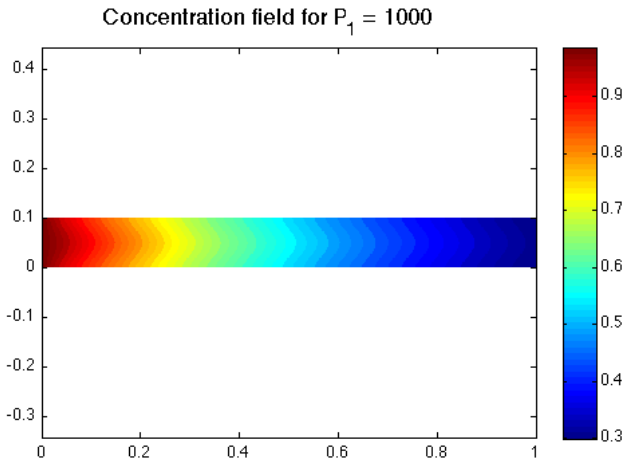

Figure 6: Concentration contours for $P_1 = 1000$

An effective way to visualize the impact of varying the inlet pressure is to plot the concentration along the horizontal line $y = H/2$. This is plotted below in figure 7. The significance of the changes in the concentration profile is explained in the following section.

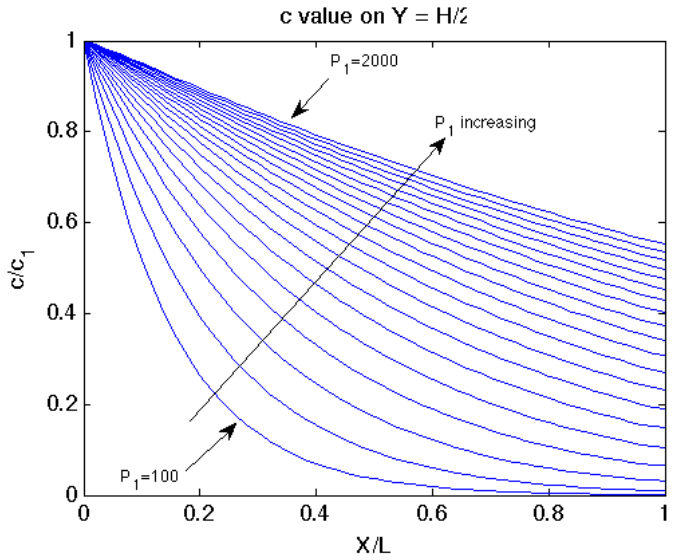

Figure 7: Concentration profiles along the line $y = H/2$ at different inlet pressures

4.4 Analyzing Battery Performance

Now that the battery system has been modeled, the results must be analyzed to determine the effects of changing the operating conditions. One way to do this is to examine various aspects of battery performance such as capacity and current generation capability. Then, a performance metric is proposed in order to determine the optimal operating conditions for the battery.

4.4.1 Battery Capacity

The most obvious effect of increasing the inlet pressure, and therefore flow rate, is that some active material is convected out of the reaction area of the battery. This can be directly interpreted as an effective loss of battery capacity. An effective capacity fraction of the battery can be defined as

$$\epsilon = 1 - \frac{\int_{outlet} c(\mathbf{x})\, dA}{\int_{inlet} c(\mathbf{x})\, dA} \tag{15}$$

This new quantity ϵ reflects the fraction of the active battery material that reacts before leaving the reaction area. A plot of the effective capacity vs inlet pressure is below in figure 8. Values range from $\epsilon = 0.9983$ at $P_1 = 100$ to $\epsilon = 0.4555$ at $P_1 = 2000$. As $P_1 \to \infty$, $\epsilon \to 0$. Using this effective capacity as the only performance metric, pumping at the lowest pressure possible would appear to give optimal performance.

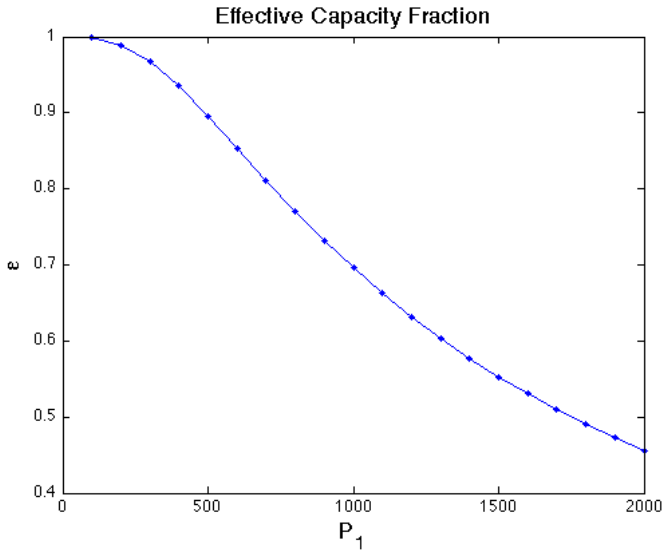

Figure 8: Plot of effective capacity fraction vs inlet pressure

4.4.2 Battery Current

Another quantity of interest is the electrical current that the battery is capable of generating. The electrical current is related to the reaction rate via Faraday's constant F.

$$I = F \cdot \int k \cdot c(\mathbf{x})\, dV \tag{16}$$

The current is plotted against the inlet pressure below in figure 9. The actual value of the current is not important since it is dependent on so many different parameters such as geometry and chemistry, which are not considered in detail due to lack of experimental information. Rather, the key feature of this plot is that the current is monotonically increasing with inlet pressure. This is not an unexpected result, since the current is proportional to the average concentration in the reaction area. This can be visually determined to be the case in figure 7. Therefore, if the ability to generate current is the only performance metric, the model predicts that optimal performance is achieved when inlet pressures are as high as possible. This puts this performance metric directly at odds with the effective capacity fraction performance metric, since what is optimal for one is the worst possible case for the other. Due to this apparent contradiction, it may be useful to define an alternative performance metric to characterize the performance of the battery.

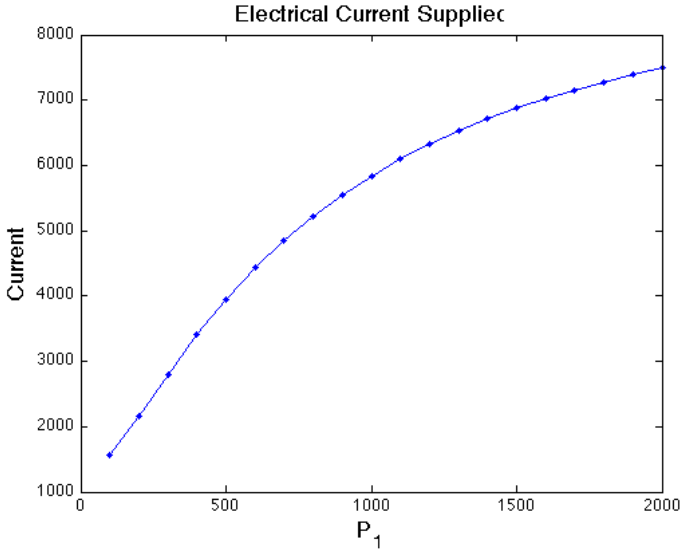

Figure 9: Current generation as a function of inlet pressure

4.4.3 Combined Performance Metric

In order to address the apparently contradictory performance metrics of effective capacity fraction ϵ and battery current I, a function to describe the performance of the battery that utilizes both conditions must be created. Since the optimal battery maximizes both ϵ and I, a simple function that could capture this behavior is

$$M(P_1) = \epsilon(P_1) I(P_1) \tag{17}$$

This function reaches its extremum when

$$\frac{dM}{dP_1} = \epsilon \frac{dI}{dP_1} + \frac{d\epsilon}{dP_1} I = 0 \tag{18}$$

Rather than evaluating the derivatives in (18), a plot of (17) was created to visually identify the maximum. This plot is below in figure 10. This plot shows that the optimal battery performance (according to this performance metric) is neither at $P_1 \to 0$, as ϵ alone would predict, nor is it at $P_1 \to \infty$, as I alone would predict. Rather, the optimum performance is around $P_1 = 1000$.

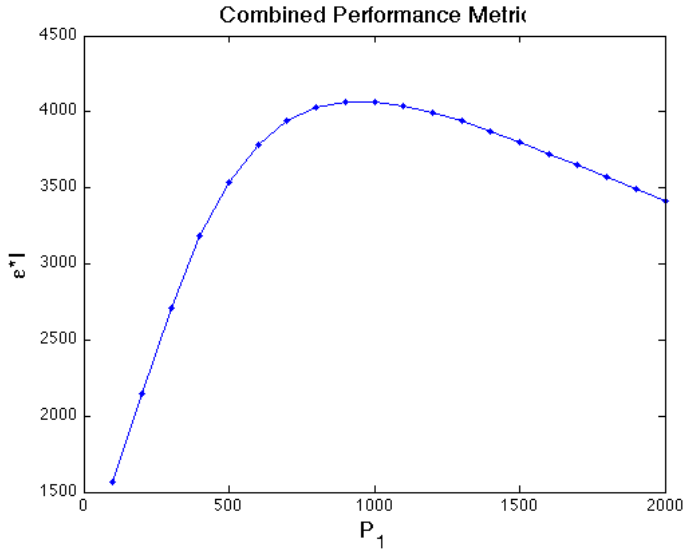

Figure 10: Plot of the combined performance metric M

5 Conclusions

In this study, a mathematical model of a flow battery was created by coupling a fluid dynamics model, the Navier-Stokes equations, with a scalar transport law. In order to investigate the behavior of the model, a finite difference solver was written to solve the coupled system of partial differencial equations. The solution to the incompressible Navier-Stokes equations was approximated using a projection method by Chorin [1]. The performance of the solver was analyzed by comparing its results to the analytical solution of 2D parallel plate pressure-driven flow and to previously published results to the lid-driven cavity flow at multiple Reynolds numbers by Ghia *et al* [2]. Once the accuracy of the fluid solver had been established, the resulting velocity field was used as the velocity field in a scalar transport

equation modeling the evolution of battery active species concentration over a rectangular domain.

The combined model was used to investigate the performance of the flow battery under varying operating conditions. Upon doing this, an apparent paradox arose in characterizing the battery performance, so a combined metric was proposed in an attempt to reconcile two otherwise contradictory performance metrics. Using this performance metric, it was shown that the battery performance was optimal at neither extreme of operating conditions, indicating that careful engineering is necessary for the optimal performance of a real battery system.

In order to improve the model, a more realistic reaction rate law could be implemented by coupling an electrostatics model with the flow and species transport models. In addition, experiments can be carried out to identify material properties such as diffusion coefficient, viscosity, density, etc.

References

[1] AJ Chorin. Numerical solution of the Navier-Stokes equations. *Mathematics of computation*, 22(104):745, October 1968.

[2] U Ghia, KN Ghia, and CT Shin. High-Re solutions for incompressible flow using the Navier-Stokes equations and a multigrid method. *Journal of computational physics*, 411:387–411, 1982.